

Outdoor scene reflectance measurements using a Bragg-grating-based hyperspectral imager

JIA ECKHARD,^{1,*} TIMO ECKHARD,¹ EVA M. VALERO,¹ JUAN LUIS NIEVES,¹ AND ESTIBALIZ GARROTE CONTRERAS²

¹Optics Department, University of Granada, ES-18071 Granada, Spain

²Computer Vision Group Tecnalia R&D, ES-48170 Zamudio, Spain

*Corresponding author: jia.eckhard@gmx.com

Received 24 November 2014; revised 13 February 2015;

accepted 23 February 2015; posted 23 February 2015 (Doc. ID 225395); published 3 April 2015

The acquisition of spectral reflectance factor image data in an outdoor environment is a challenging task, mostly due to nonstatic scene content and illumination. In this work, we propose a work-flow for this task using a commercial Bragg-grating-based hyperspectral imager that can capture the visible and near-infrared part of the light spectrum. To our knowledge, we are the first who use this technology for outdoor spectral reflectance factor imaging. The work-flow involves focus position and exposure time estimation, illumination scaling, and image registration, among other procedures. Most of them generally apply to hyperspectral imaging, while some are specific to a Bragg-grating-based hyperspectral imaging device when dealing with specific challenges in outdoor environments. We have conducted some experiments to evaluate the quality of the acquired image data and discussed some limitations of the technology for spectral imaging of outdoor scenes. Fourteen urban scene spectral images acquired using the proposed approach are already publicly available to the scientific community under a Creative Commons license. © 2015 Optical Society of America

OCIS codes: (110.4234) Multispectral and hyperspectral imaging; (100.2000) Digital image processing.

<http://dx.doi.org/10.1364/AO.54.000D15>

1. INTRODUCTION

In recent years, hyperspectral imaging has drawn increasing attention in a wide range of fields such as astronomy, agriculture, and medicine [1–3]. A hyperspectral image of n bands with spatial resolution of $r \times c$ can be represented as a three-dimensional (3D) data cube $\mathbf{C} = [C(x, y, \lambda)]_{r \times c \times n}$, where x and y represent the spatial dimensions of the image, and λ represents the spectral dimension (usually comprising a range of consecutive wavelengths). In most cases, the image intensity corresponds to either the spectral radiance or spectral reflectance factor [4]. Generally, hyperspectral cameras sense scene radiance, and the reflectance factor data is computed by accounting for the spectral power distribution of the scene illumination.

Most hyperspectral imaging devices use one of the following techniques: spatial scanning (e.g., a line-scan hyperspectral imager), spectral scanning (e.g. a liquid-crystal tunable filter hyperspectral imager), one-shot (e.g., a computed tomography imaging spectrometer), or spatio-spectral scanning (e.g., an imaging system using slit spectroscopy or a Bragg-grating-based hyperspectral imager) [5–7]. Figure 1 illustrates the four techniques schematically by showing in color the data that

is acquired in one shot. Using any of these approaches, hyperspectral images can be acquired either in an indoor environment with controlled illumination [8] or an outdoor environment under daylight [4]. In the case of outdoor hyperspectral imaging, varying daylight illumination has to be taken care of [9].

In this paper we introduce the acquisition of hyperspectral reflectance factor images of outdoor scenes using a volumetric Bragg-grating-based spatio-spectral scanning device: hyperspectral camera V-EOS by Photon Etc. (later on denoted as HI) [10], covering the visible and near-infrared spectrum. With accurate device characterization and sophisticated data processing, it is possible to acquire hyperspectral images of a wide spectral range with high spatial and spectral resolution.

The HI has been used in applications related to mining, oil and gas operations, dermatology, and agriculture, with controlled illumination and static scene content [10]. As an addition to these applications, we used it for acquiring outdoor hyperspectral image data which is extra challenging because the radiometric conditions of the image scene are generally not static and the illumination does not have a smooth spectrum. Therefore, additional measures for dealing with these issues are required. By providing a detailed work-flow of the

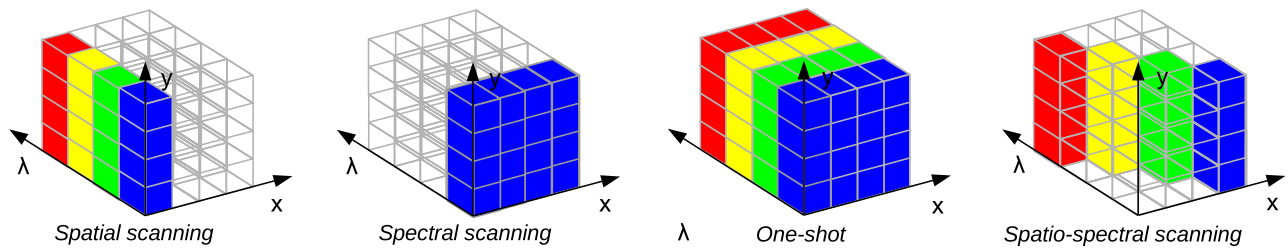


Fig. 1. Illustration of the acquisition process in one shot in the four hyperspectral imaging techniques.

image cube acquisition and post-processing for reflectance factor imaging of outdoor scenes, this paper targets readers from the scientific community as well as engineers using similar technologies for hyperspectral imaging. To our knowledge, we are the first who use this technology for outdoor spectral reflectance factor imaging. Some solutions for dealing with the challenges in outdoor hyperspectral imaging as well as the whole work-flow are therefore novel or have not been thoroughly explained in the literature.

We continue the paper with an introduction of the Bragg-grating-based hyperspectral imaging technique in Section 2. Afterward follows the acquisition work-flow and corresponding discussion on specific procedures to account for nonstatic radiometric scene conditions in Section 3. We further illustrate the data post-processing in Section 4. The evaluation and limitations of the images acquired are presented in Section 5. In Section 6, we introduce our publicly available image database of the hyperspectral image cubes acquired in accordance with the procedures introduced in this paper. Finally, we summarize the most relevant conclusions of this work in Section 7.

2. BRAGG-GRATING-BASED HYPERSPECTRAL IMAGER

A. V-EOS Hyperspectral Camera: HI

The HI used in this work is a volumetric Bragg-grating-based hyperspectral imager. It is able to acquire hyperspectral image data from 400 to 1000 nm with spectral resolution of 2 nm. It achieves this wide spectral range by using two volumetric gratings with different modulation periods: one for the visible and

the other for the near-infrared spectral range (Grating 1 covers 400–640 nm and Grating 2 covers 650–1000 nm). The spatial resolution of this device is 1392 pixels \times 1040 pixels.

A schematic illustration which depicts the most important optical components inside the device is shown in Fig. 2. We discuss in the following subsections relevant information about the general function principle, the sampling, and resampling scheme of the HI. For a more detailed description of Bragg-grating-based spectral filtering, the reader may refer to [7,11,12].

B. Volumetric Bragg Grating

A volumetric Bragg grating consists of a volume in which the refraction index varies periodically. Depending on the orientation of the modulation structure with respect to the incident light angle, the grating acts as a tunable spectral filter which transmits only a narrow band of the electromagnetic spectrum, centered on wavelength λ

$$\lambda = 2\Lambda \sin(\theta), \quad (1)$$

where Λ is the refraction index modulation period, and θ is the incident light angle in the modulating medium [7].

Due to the volumetric nature of the grating, spectral filtering of scene radiance occurs in one spatial dimension of the image. In our acquisition, for example, different columns in the acquired radiance intensity image correspond to different wavelengths and the wavelength λ_x for column x is

$$\lambda_x = 2\Lambda \sin(\theta + \alpha_x), \quad (2)$$

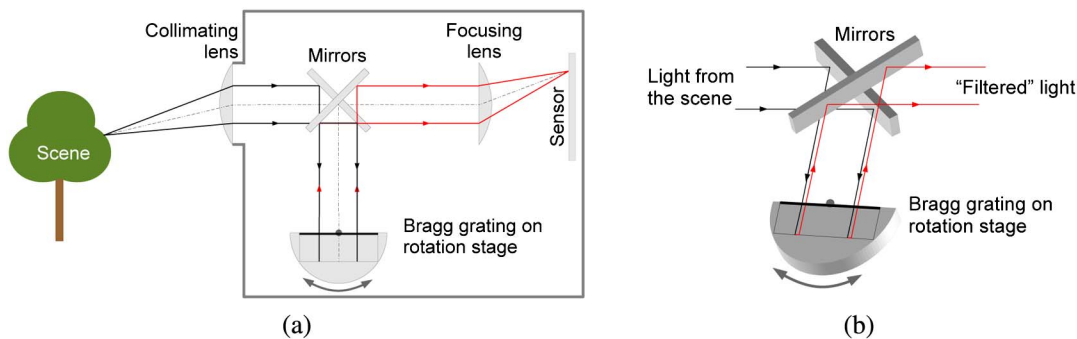


Fig. 2. (a) Schematic illustration of the HI (depicting only one Bragg grating); (b) 3D view of the interaction between light and mirrors and the Bragg grating. Note that the light rays' paths in this figure are depicted for illustration purposes, and do not necessarily correspond to real trajectories.

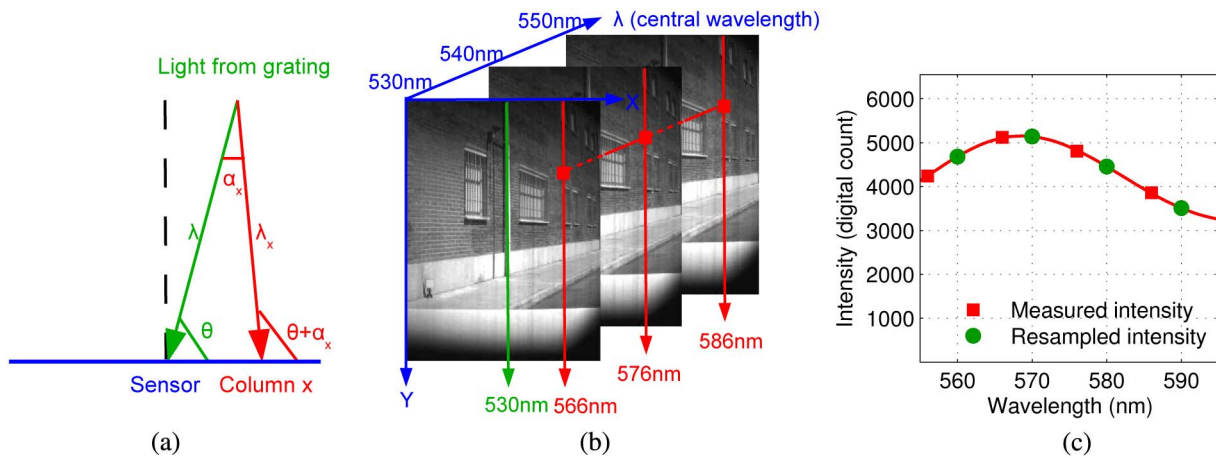


Fig. 3. (a) Relation of wavelength and incidence angle in the Bragg-grating-based imaging process; (b) column-dependent wavelength information in the acquired raw images; (c) interpolation process in image resampling.

where θ is the central wavelength incident angle and α_x is the angle offset for column x [Fig. 3(a)].

Rotating the grating results in a modulation of the filter function at each pixel location in the image. Correspondingly, it is possible to acquire a set of images that sample the scene radiance with high spectral resolution.

C. Sampled Spatio-Spectral Image Data and Image Resampling

A raw image cube captured by a volumetric Bragg-grating-based hyperspectral imager contains images of spatially varying spectral content. We refer to the spatio-spectral image that contains varying spectral information as raw image, and the wavelength corresponding to the central column in the image as central wavelength. As introduced in the previous subsection, the functional relation of image band, spatial location, and corresponding filter wavelength are known. By image cube resampling, it is possible to obtain a spectral image cube in which each image band corresponds to a particular wavelength. The manufacturer denotes this process as image rectification. We refer to the resampled image as rectified image.

An important consideration in the resampling process is the spectral sampling rate. Our most common configuration for

outdoor scene acquisition is spatio-spectral scanning with 10 nm step spectral sampling, which means that the central wavelength of successive images in a cube varies by 10 nm. As the spectral information measured varies with pixel location (in column), we do not have information for all the wavelengths that we aim to acquire, but some intermediate values [Fig. 3(b)]. Data resampling accounts for this by interpolating the missing values [Fig. 3(c)]. However, there are limitations of this signal reconstruction scheme which can be explained by the Nyquist–Shannon sampling theorem [13], stating that signals with higher frequency than half the sampling rate cannot be fully recovered.

The consideration of the sampling rate is important in outdoor imaging because the spectral power distribution (SPD) curve of the daylight that illuminates the scene is not smooth. It is caused by chemical elements’ absorption behavior in the Earth’s atmosphere [14]. Figure 4(a) shows the daylight SPD measured by a PR-745 SpectraScan spectroradiometer by Photo Research Inc. on a clear day in Granada, Spain. We can see that there is strong absorption at 760 nm which is due to the gaseous absorber O_2 . In our case, the corresponding rapid signal change results in an under-sampling artifact in the rectified image which is visible as columnwise stripes.

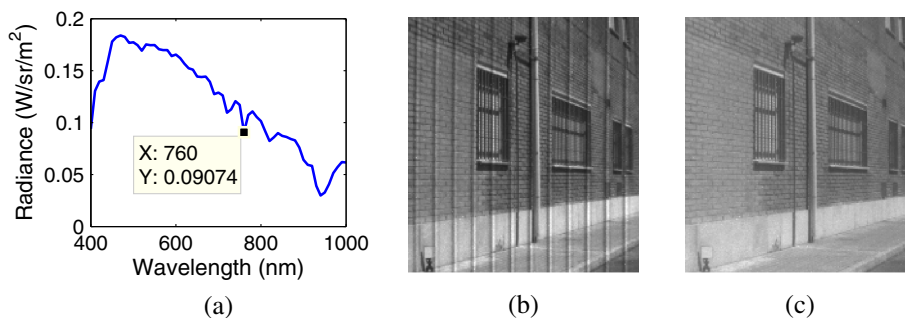


Fig. 4. (a) Spectral power distribution of daylight measured by a PR-745 spectroradiometer on a clear day in Granada, Spain; (b) rectified and flat-fielded image of 760 nm captured with sampling rate of 10 nm with the artifact of columnwise stripes; (c) image captured with sampling rate of 1 nm without artifact.

This effect cannot be fully compensated by flat-field correction (FFC; Section 4, Subsection B). Therefore, the sampling rate for outdoor acquisition has to be adjusted for the strong absorption band image (specially for the O₂ absorption band at 760 nm) to avoid this artifact. We illustrate in Figs. 4(b) and 4(c) the rectified and flat-fielded image of 760 nm captured by sampling rate of 10 and 1 nm. We can see that in the first image the artifact of columnwise stripes is clearly visible, while in the second one this artifact is not present anymore. A more detailed description of the solution for this under-sampling problem can be found in Section 3, Subsection B.

3. HYPERSPECTRAL IMAGE ACQUISITION

For each acquisition, a scene cube (with a scene of interest as image content), a white cube (with a spatially uniform target as scene content, used for FFC), and two dark cubes (void of scene radiance reaching the camera sensor, used for dark current correction for the scene cube and the white cube) have to be acquired.

Successful spectral image acquisition in outdoor environment further requires specific procedures to account for the typically dynamic scene illumination conditions. We discuss these procedures and introduce our proposed acquisition work-flow in the following subsections.

A. Acquisition Setup and Required Tools

For an ideal capture, scene content and scene illumination should remain static throughout the entire acquisition time (which in our case could be up to 0.5 h). It shall be noted that not only scene objects, but also shadow casts should remain static. For the illumination, both the radiometric properties and spatial distribution over the scene should not change. This ideal condition is generally not available when daylight is considered as scene illumination because of the change in the apparent position of the Sun due to the Earth's rotation. However, depending on geographic location and local weather conditions, the most static environmental conditions can be selected. We consider the midday time (when the sun is at its zenith) in a clear day as such.

Figures 5(a) and 5(b) show the setup for acquiring the white cube and scene cube. Figure 5(c) shows the color-rendered image (under CIE Standard Illuminant D65 with the CIE 1931

2° Standard Observer) of a hyperspectral image cube of a scene using this setup (after post-processing). Dark cubes are acquired by simply putting on the lens cap. The required tools are one focusing target plate and two white reference plates with Lambertian surface.

The focusing target plate is approximately 40 cm × 40 cm in size and is used for focusing the imaging system. After focusing, we remove it from the scene before starting capturing the scene cube and white cube. The pattern on the target plate can be any shape which has good contrast against a homogeneous background (in our case a black cross on a white background). We focus on this square region instead of an arbitrary scene region, because images captured at different focusing positions are slightly displaced, which can cause miscalculation of the optimal focus position. For the same reason, the focusing pattern does not fill up the background so that it does not move out of the focusing region due to image displacement.

The White Plate 1 we used is a Zenith Lite diffuse reflectance target (95% Reflectance) by SphereOptics. It is of size 20 cm × 20 cm and is used for calculating exposure times (Section 3, Subsection D), FFC (Section 4, Subsection B), and illumination scaling (Section 4, Subsection C). We put White Plate 1 close to the camera system and cover the entire field of view when acquiring the white cube. The white plate is much closer to the camera than the scene and therefore is out of focus. For FFC this can be an advantage because the image blur reduces visibility of imperfections on the plate. When acquiring the scene cube, we move down White Plate 1 and cover the bottom part of the field of view so that only a white stripe appears in the captured scene. The image region corresponding to this stripe is later on used for illumination scaling, explained in Section 4, Subsection C. After these post-processing steps, we crop the image to remove this part from the scene.

The White Plate 2 we used is a SRT-99-050 reflectance target by Labsphere. It is of size 10 cm × 10 cm with known spectral reflectance information specified by the manufacturer [Fig. 5(d)]. It is used for reflectance normalization (Section 4, Subsection D). It is important to use White Plate 2 (placed in the scene) for reflectance normalization instead of White Plate 1 (placed close to the camera), because the illumination

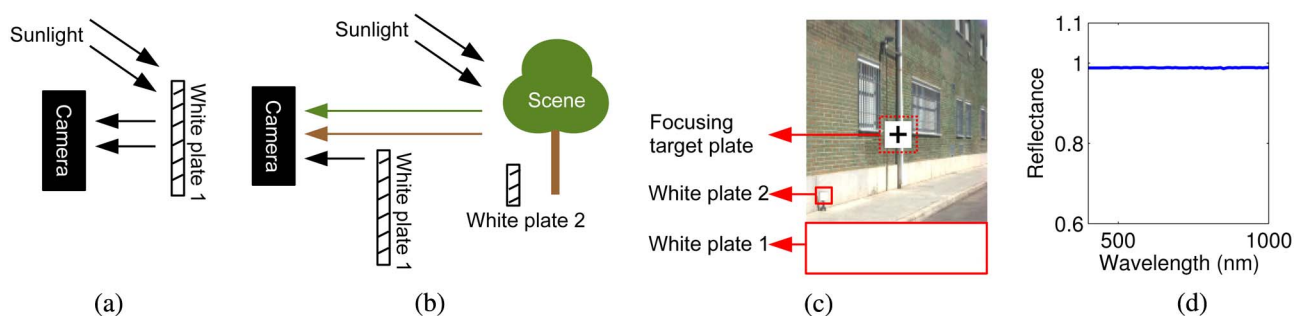


Fig. 5. (a) Setup for capturing the white cube; (b) setup for capturing the scene cube; (c) color-rendered image of an outdoor scene cube captured with this setup (after post-processing, with focusing target plate placed in temporarily); (d) spectral reflectance of White Plate 2 specified by the manufacturer.

condition of White Plate 1 and the scene might not be the same.

B. Optical Setup: Camera and Filter Parameters

In general, the most important parameters related to the optical system are aperture size, exposure time, and focus position. Exposure time and focus position estimation are discussed in detail in the following subsections. The aperture size influences the exposure time, depth of field, and the optimal focus position; in composite, the sharpness of the image. We heuristically selected a minimal aperture size so that the required exposure time is reasonably short and the depth of field is large enough to allow a relaxed focus setting (for different wavelengths and scene distances).

As the volumetric Bragg grating is essentially an optical spatio-spectral image filter, the corresponding filter parameters that have to be adjusted are the spectral range and sampling interval for which image data is to be acquired. We consider the range of 400–1000 nm (which is the maximum spectral range for the device) with 10 nm sampling, and it results in a total of 61 images per cube.

The spectral range within a raw image captured by Grating 1 is $[\lambda - 50, \lambda + 50]$ nm, and by Grating 2 is $[\lambda - 70, \lambda + 70]$ nm, where λ is the central wavelength. Accordingly, the actual number of raw images that needs to be acquired to obtain a spectral cube in the desired range is 85 (raw images corresponding to 350–690 nm central wavelength from Grating 1 and 580–1070 nm central wavelength from Grating 2).

In order to avoid the “stripe artifact” in the 760 nm image caused by under-sampling (Section 2, Subsection C), we acquire raw images from 690 to 830 nm in steps of 1 nm. To reduce the acquisition time, we acquire these images with only 10% of the exposure time initially assigned for the 760 nm image. The sum of the resulting 10 rectified images from 756 to 765 nm corresponds to the finer-sampled 760 nm image.

C. Focus Position Estimation

The optimal focus position for acquiring a scene changes with the distance between the scene and the camera, the aperture size, and the wavelength. For a fixed aperture size, theoretically we would need to use a different focus position for each wavelength and scene distance. However, it is not very practical to find the optimal focus position for each of the 85 central wavelength bands, as the focusing routine requires acquisition of several images at different focus positions of the motorized lens (11 images in our case). Further, image registration also depends on the focus position, as we will discuss later on. As we set the aperture size to a small value to have a large depth of field, we can use the same focus position setting for acquiring images of different central wavelengths from the same grating. Consequently we only need to find two optimal focus positions for the two gratings when we acquire scenes at different distances. In our acquisition procedure, we use images of central wavelength 540 and 740 nm as representatives for finding optimal focus positions for Grating 1 and Grating 2, respectively.

To find the optimal focus, we place the focusing target plate temporarily in the scene and acquire a set of images using a

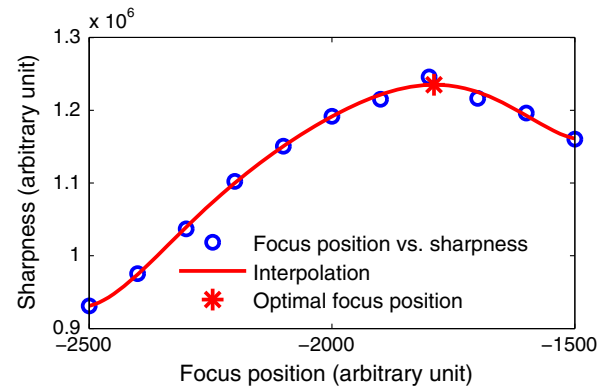


Fig. 6. Example plot of sharpness versus focus position.

sequence of focus positions. Then we calculate the sharpness of the same square area that bounds the focus target in each image, plot sharpness against focus position and fit with a polynomial function. At last, we select the optimal focus position that corresponds to the maximum sharpness value (Fig. 6).

There are many focus measures available from the literature, and the performance often depends on their particular application. In our work, we have tested all the focus measures mentioned in the study by S. Pertuz *et al.* [15], and selected one based on the magnitude of image gradient defined as [16]

$$f(I) = \frac{1}{rc} \left(\sum_{i,j \in \Omega_I} (G_x(i,j)^2 + G_y(i,j)^2) \right), \quad (3)$$

where $r \times c$ is the spatial resolution of the image I (in our case it is the image region which contains the focusing target), G_x and G_y are the X and Y image gradients computed by convolving the image with Sobel operators, and Ω_I is the image coordinate domain.

Rapid illumination change or movement of the system during the process of finding the optimal focus positions influence the focus measure and therefore have to be avoided.

D. Exposure Time Estimation

Too long exposure time leads to difficulties in maintaining the acquisition conditions stable (illumination, scene content, and so on), high noise level, and overexposure. Too short exposure time results in low utilization of the camera’s dynamic range and also high noise level. We need to find a compromise between having a short exposure time and making good use of the dynamic range. As a trade-off, we use only 40% of the dynamic range of the camera. This means that the exposure time is selected such that the camera response for a diffuse white surface included in the scene does not exceed the threshold intensity $i_{th} = (2^{14} - 1) \times 0.4 = 6553.2$ counts for the 14 bit sensor of the HI.

In this camera system, the imaging efficiency varies with central wavelength, thus we estimate the exposure time for each raw image. The estimation is based on the following linear relation of exposure time t and maximum intensity i in the acquired image

$$i = kt + i_0, \quad (4)$$

where scalar k is the slope parameter and i_0 is the image intensity offset at zero exposure. The pseudocode for estimating exposure time is illustrated in Algorithm 1. The basic idea is to capture two test images using short exposure times, fit Eq. (4), and obtain k and i_0 . Then the exposure time for any desired image intensity level (eg. the threshold intensity i_{th}) can be estimated using Eq. (4).

Algorithm 1: Pseudocode for Exposure Time Estimation

```

Input: Initial exposure time  $t_{init}$ , minimum exposure time of the
camera  $t_{min}$ , intensity threshold  $i_{th}$ , saturation level  $i_{sat}$ 
Output: Estimated exposure time  $t$ 
 $I_1 \leftarrow \text{AcquireImage}(t_{min});$ 
 $i_1 \leftarrow \text{Max}[\text{MedianFilter}(I_1)];$ 
 $I_2 \leftarrow \text{AcquireImage}(t_{init});$ 
 $i_2 \leftarrow \text{Max}[\text{MedianFilter}(I_2)];$ 
while  $i_2 < i_1 + 0.25i_1$  or  $i_2 > i_{sat}$ 
  if  $i_2 < i_1 + 0.25i_1$  //image intensity too low
     $t_2 \leftarrow 2t_2;$  //double exposure time
  else //image intensity too high
     $t_2 \leftarrow 0.5t_2;$  //half exposure time
  end
   $I_2 \leftarrow \text{AcquireImage}(t_2);$ 
   $i_2 \leftarrow \text{Max}[\text{MedianFilter}(I_2)];$ 
end
 $k \leftarrow \frac{i_2 - i_1}{t_2 - t_1}$  //calculate the slope
 $i_0 \leftarrow i_1 - kt_1$  //calculate the intercept
 $t \leftarrow \frac{i_{th} - i_0}{k}$  //calculate the exposure time

```

In the algorithm, the initial exposure time t_{init} for all the wavelengths is set to 0.1 s, which is a value heuristically found to be proper in our case. The maximum image intensity i is found from the image region corresponding to White Plate 1 [the white stripe in Fig. 5(c)] instead of the whole image, which might contain specular reflections. Further, to make the approach more robust against noise, we apply a 3×3 median filter to the image before finding the maximum intensity.

Following this approach, the total capture time for acquiring 85 raw images for one cube in our case is about 30 min (including the procedure of estimating exposure times). Figure 7 shows the exposure times estimated for a typical outdoor scene acquisition and the maximum intensities of the corresponding acquired raw images. The maximum exposure time is limited to

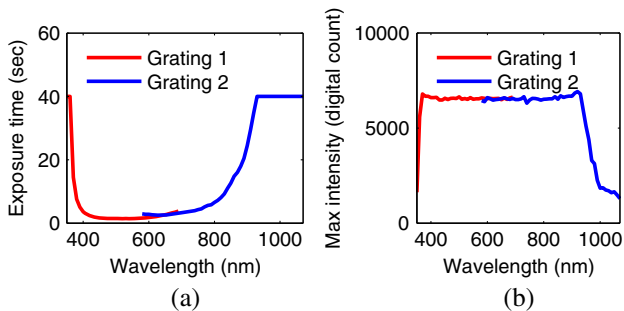


Fig. 7. (a) Exposure times calculated for a typical outdoor scene; (b) maximum intensities of the corresponding acquired raw images.

40 s even though i_{th} is not reached for the first and last several bands. The sensitivity for these bands is so low that very long exposure times are needed to reach i_{th} . But then the images will be degraded heavily by noise and the quality will be below a useful level. In the end, the low signal level in these image bands results in higher noise level than other bands.

E. Summary of the Acquisition Work-Flow

The following list of consecutive steps summarizes the spectral image cube acquisition work-flow.

- Find the focus positions for Grating 1 and Grating 2.
- Acquire the scene cube C_s . The set of exposure times t_s is estimated before each image capture.
- Acquire the white cube C_w with another set of exposure times t_w estimated during acquisition. We use different exposure times for acquiring the scene cube and white cube to avoid underexposure or saturation that might occur due to illumination change.
- Acquire the two dark cubes C_{sd} and C_{wd} using exposure times t_s and t_w , respectively. As the dark current changes with temperature [17], it is favorable to acquire the dark cubes right after the acquisition of scene cube and white cube rather than at a later moment with different ambient temperature.

4. IMAGE DATA POST-PROCESSING

A. Dark Current Correction

Dark current is a source of noise intrinsic to the CCD [17]. It is not uniform for all pixels, and it depends on sensor temperature and exposure time. In our study, we correct dark current for the scene cube and white cube by subtracting the corresponding dark cubes.

B. Flat-Field Correction

Figure 8 shows the intensities of the rectified image of 600 nm acquired by pointing the camera into an integrating sphere illuminated by a Philips PF308 E27/240V/500W incandescent lamp, before and after FFC. For a perfectly uniform imaging system, image intensities would be constant at every pixel location. What we can observe in the intensity image without FFC is a strong nonuniformity pattern due to photo response nonuniformity of the sensor and nonuniformities of the optical elements in the device. The nonuniformity pattern is wavelength-dependent, which requires FFC for each image band. A simple yet effective way is to divide the scene cube

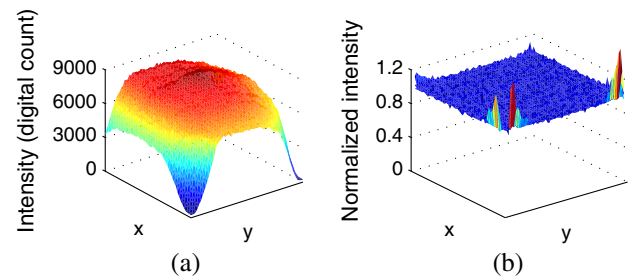


Fig. 8. Image intensities of the rectified image of 600 nm, resulting from pointing the HI into a white integrating sphere; (a) before FFC; (b) after FFC.

by the white cube on a pixel-by-pixel basis (after dark current correction) [18].

C. Illumination Scaling

In outdoor capture, the daylight SPD can change between capturing the scene cube and white cube, leading to erroneous FFC results. Because of the spatio-spectral nature of the imaging process, illumination scaling has to be done by multiplying the (dark current corrected and flat-fielded) image data columnwise by a set of scaling factors. For a raw spectral data cube of size $1392 \times 1040 \times 61$, there are 61 sets of scaling factors (one per image), each containing 1040 values (one per column). The scaling factor for column j ($j = 1, 2, \dots, 1040$) in image band λ ($\lambda = 400, 410, \dots, 1000$ nm) are calculated by

$$\alpha(j, \lambda) = \frac{W_w(j, \lambda)}{W_s(j, \lambda)}, \quad (5)$$

where W_s and W_w are the rowwise mean intensity of the white stripe region in the scene image and the corresponding area in the white cube image (after dark current correction and FFC).

D. Reflectance Normalization

The illumination of the scene might vary from the illumination on White Plate 1 (used for FFC and illumination scaling). This variation can be corrected by normalizing the image data against the image region corresponding to White Plate 2. We accomplish this by dividing each (dark current corrected, flat-fielded, and illumination-scaled) image band λ by $\beta(\lambda)$, which is the average intensity of the White Plate 2 region in the same image. Then we multiply each image band pixelwise by $r_w(\lambda)$, which is the reflectance of White Plate 2 at wavelength λ [Fig. 5(d)]. Note that this approach will not account for local scene illumination variations.

E. Image Registration and Distortion Correction

The unprocessed images acquired by the HI show a barrel-shaped distortion pattern at each image channel. It is introduced by the optical components of the camera, consisting of a zoom lens, a collimating and focusing lens, various mirrors, and the volumetric Bragg gratings. The distortion effect is further coupled with a wavelength-dependent image misalignment.

Registration and distortion correction is the process of aligning each image in the cube spatially to its reference image, which is free of distortion and misalignment. The problem to be solved is finding out the amount of displacement between the unregistered and registered image for each pixel, and moving the pixels in the unregistered image to the "correct" location corresponding to the registered image.

We recently proposed a solution to this nonrigid registration problem using a free-form deformation model of multilevel refined uniform cubic B-splines. The idea is to track the displacement of some key pixels in the scene and fit a B-splines model to the displacement field. Then the displacement value at each pixel position is interpolated by the fitted model. A registration accuracy of approximately one pixel was achieved for the HI with this method. For more details, the reader can refer to [19].

F. Summary of the Image Post-Processing

The post-processing steps can be expressed in the following equation [for the pixel with spatial coordinate (i, j) at image band λ]

$$R_s(i, j, \lambda) = f\left(\frac{C'(i, j, \lambda)}{\beta(\lambda)} \times r_w(\lambda)\right), \quad (6)$$

where C' is the scene cube after dark current correction, FFC and illumination scaling, and is defined by

$$C'(i, j, \lambda) = \frac{C_s(i, j, \lambda) - C_{sd}(i, j, \lambda)}{C_w(i, j, \lambda) - C_{wd}(i, j, \lambda)} \times \alpha(j, \lambda), \quad (7)$$

where C_s , C_w , C_{sd} and C_{wd} are the acquired scene cube, white cube, dark cubes for the scene cube and white cube, and α is the set of illumination scaling factors. β is the set of average intensities for all wavelength bands in the image area corresponding to White Plate 2 in C' . r_w is the spectral reflectance of White Plate 2. f denotes the function for image registration and distortion correction. R_s is the cube of spectral reflectance factor data that we aim to acquire.

5. MEASUREMENT PERFORMANCE EVALUATION AND LIMITATIONS

In order to evaluate the colorimetric and spectral accuracy of the image data captured by the HI with our proposed workflow, we acquired two image cubes of the ColorChecker 24 Patch Classic target on a sunny day and a partial sunny day with moving clouds. The cloudy condition is far from ideal but good for illustrating the performance of our framework. We also measured the spectral reflectances of the ColorChecker using the PR-745 spectroradiometer (indoor with incandescent light as illumination) for comparison. Accordingly, we have four sets of reflectance measurements of the 24 color patches in the ColorChecker, denoted by:

- R_0 , measured by the PR-745 spectroradiometer.
- R_1 , measured by the HI without illumination scaling on a cloudy day.
- R_2 , measured by the HI with illumination scaling on a cloudy day.
- R_3 , measured by the HI with illumination scaling on a sunny day.

Figure 9 shows two color-rendered images (using CIE 1931 2° Standard Observer and CIE Standard Illuminant D65) of the hyperspectral image cube captured by the HI on a cloudy day before and after image registration and illumination scaling. We can see that without these post-processing steps, the rendered image is geometrically distorted and miscolored, and from the zoomed image we can see color fringes caused by channel misalignment in the uncorrected hyperspectral cube.

Figure 10 shows the plots of R_0 , R_1 and R_2 . CIEDE2000 color difference (ΔE_{00}) [20] and goodness-of-fit coefficient (GFC) [21] values, which are used for numerical colorimetric and spectral comparison between R_0 and R_2 , are also shown above each plot of Fig. 10. Table 1 shows the numerical comparison between R_0 and the other three sets of measurements. Note that the number of significant digits does not indicate the precision of the measurements. From the results we can see that

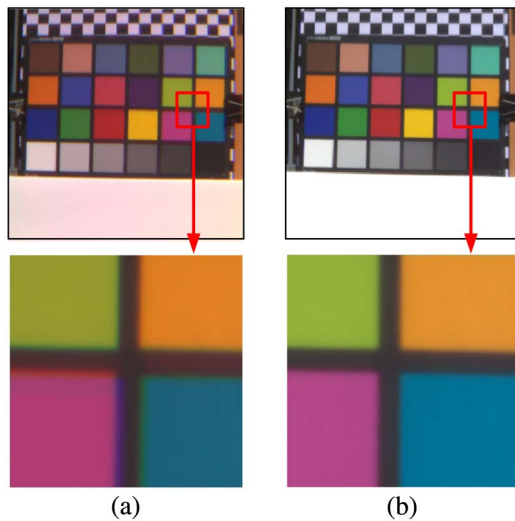


Fig. 9. Color-rendered images of a hyperspectral image cube of the ColorChecker; (a) before image registration and illumination scaling; (b) after image registration and illumination scaling.

with illumination scaling, the measurements of the two devices are more similar, and there is a good agreement in shape between \mathbf{R}_0 and \mathbf{R}_2 . Without illumination scaling, the spectra look spiky and erroneous. The measurements by the HI on a sunny day coincide better with those by the PR-745 spectroradiometer than on a cloudy day. In general, some differences between measurements by the two devices

are expected because of the difference in measurement geometry.

From Fig. 10 we can see a flaw of the measurements by the HI: there is a discontinuity between measurement from Grating 1 (400–640 nm) and Grating 2 (650–1000 nm). This phenomenon is most obvious for the last three patches. We have investigated this problem and identified a spatial crosstalk effect that depends on spatial location and image content. So far, we cannot correct it.

Another limitation of the measured spectral data comes from nonstatic scene content. Shadows, clouds, and tree leaves that are moving during the capture can result in blur or color fringes in corresponding areas in the rendered image. Figure 11 shows the color-rendered image of a hyperspectral image cube with clouds in the scene, and we can see the color fringes in the zoomed image.

6. DATABASE

We have started the creation of a database of spectral reflectance factor image cubes, acquired in accordance with the work-flow proposed in this work. The cubes are rendered publicly available under a Creative Commons license and are accessible via the webpage of the University of Granada Color Imaging Lab [22].

At this point, the database contains 14 scenes of urban environments, some of which are illustrated in Fig. 12. Another rendered scene and corresponding plots of sample spectral data are illustrated in Fig. 13. The spatial resolution of most of the images is 1000 pixels \times 900 pixels, and the spectral range is from 400 to 1000 nm in 10 nm intervals.

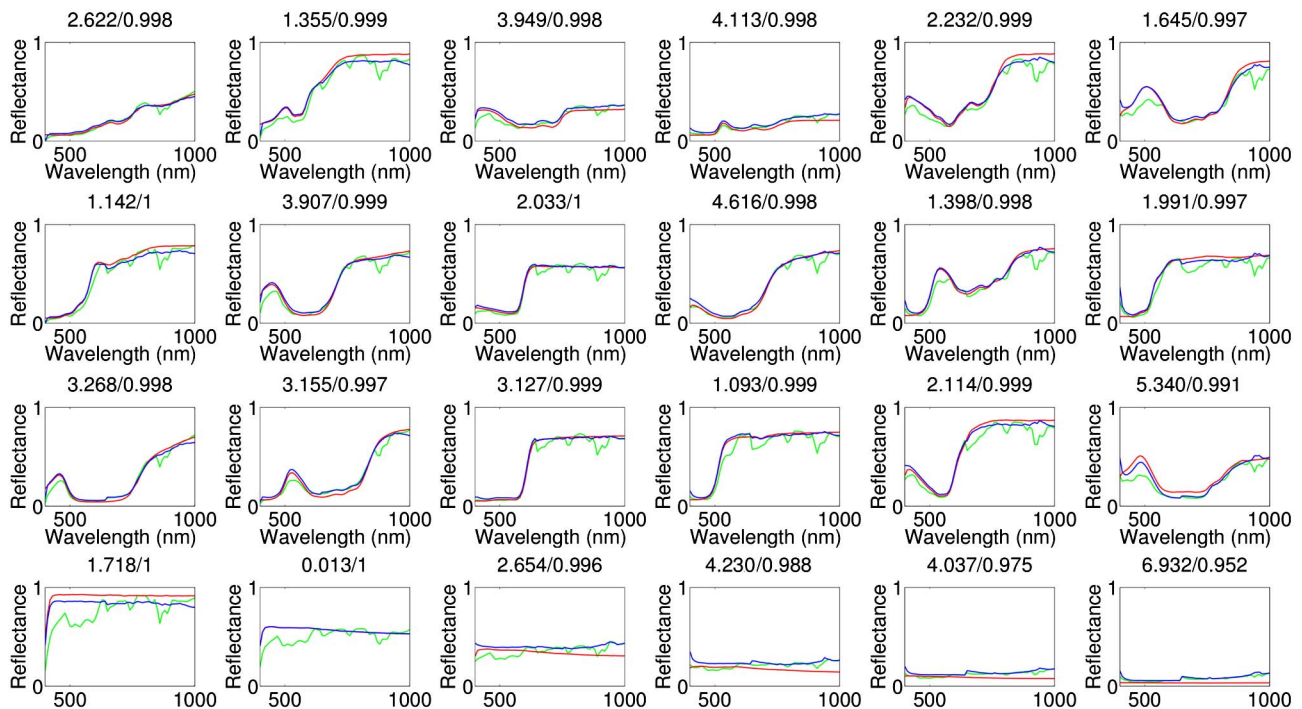


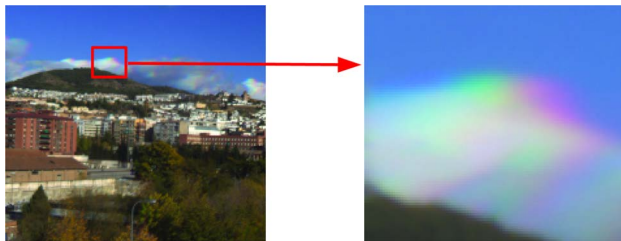
Fig. 10. Reflectance factor measurements of the 24 color patches in the ColorChecker by the PR-745 spectroradiometer (\mathbf{R}_0 , red curve) and the HI without illumination scaling (\mathbf{R}_1 , green curve) and with illumination scaling (\mathbf{R}_2 , blue curve). Numerals above each plot show the ΔE_{00} and GFC values between \mathbf{R}_0 and \mathbf{R}_2 .

Table 1. First-Order Statistics of ΔE_{00} and GFC between the Four Sets of Reflectance Measurements^a

	ΔE_{00}				Goodness-of-Fit Coefficient			
	Avg.	Max.	Min.	Std. ^b	Avg.	Max.	Min.	Std. ^b
R_0 versus R_1	6.897	12.692	1.321	3.211	0.989	0.997	0.948	0.033
R_0 versus R_2	2.862	6.932	0.013	1.576	0.995	1.000	0.952	0.019
R_0 versus R_3	2.095	5.831	0.001	1.465	0.995	1.000	0.922	0.016

^aNote that the number of significant digits does not indicate the precision of the measurements.

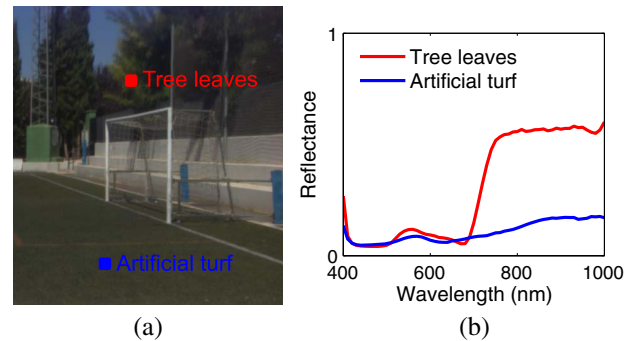
^bStd = standard deviation.

**Fig. 11.** Color-rendered image of a hyperspectral image cube and its zoomed version.

Due to the long acquisition time required for capturing a hyperspectral image cube and nonstatic scene content, the images show some unavoidable artifacts, for example, high noise level in the first and last several bands and color fringes around moving shadows and clouds.

7. SUMMARY

We have introduced the acquisition of hyperspectral reflectance factor images in outdoor environment using a volumetric Bragg-grating-based hyperspectral imager: HI. A detailed work-flow of the image cube acquisition and post-processing was proposed to deal with image nonuniformity, distortion, misalignment, and illumination change during the capture. The hyperspectral image data of the ColorChecker Classic target acquired with this work-flow shows a significant improvement in colorimetric and spectral quality compared with the data acquired without the suggested processing procedures. There is a reasonable agreement between spectral measurements of the ColorChecker using the HI and a PR-745 spec-

**Fig. 13.** Two sample spectra from one of the scenes included in our database.

roradiometer, considering that the measurements from these two devices correspond to different measurement geometries.

We have started the creation of a publicly available database of hyperspectral images of outdoor scenes. In this process, we concluded that the main advantage of the HI is its capability to yield high spatial and spectral resolution due to its spatio-spectral scanning feature. However, apart from the common problems for all the hyperspectral imaging techniques in outdoor environment due to nonstatic scene content and illumination, it brings up extra challenges, such as the under-sampling artifact due to absorption bands (Section 2, Subsection C), as well as the illumination scaling problem (Section 4, Subsection C). We proposed solutions to these problems and illustrated that our proposed work-flow makes spectral reflectance factor imaging in outdoor environment feasible with this device technology.

**Fig. 12.** Color-rendered images of four of the scenes included in our database.

This work has been financed by a joint agreement (Reference Number C-3368-00) between Tecnalia Corporation and the Fundación General UGR-Empresa from Spain. We would like to acknowledge Marc Verhaegen and Brice Bourgoïn from Photon Etc. for their valuable feedback and support with respect to this work.

REFERENCES

1. L. Pasquini, G. Avila, E. Allaert, P. Ballester, P. Biereichel, B. Buzzoni, and S. Zaggia, "FLAMES: a multi-object fiber facility for the VLT," *Proc. SPIE* **4008**, 129–140 (2000).
2. F. M. Lacar, M. M. Lewis, and I. T. Grierson, "Use of hyperspectral imagery for mapping grape varieties in the Barossa Valley, South Australia," *Proc. IEEE* **6**, pp. 2875–2877 (2001).
3. Z. Liu, J. Yan, D. Zhang, and Q. Li, "Automated tongue segmentation in hyperspectral images for medicine," *Appl. Opt.* **46**, 8328–8334 (2007).
4. D. H. Foster, K. Amano, S. Nascimento, and M. J. Foster, "Frequency of metamerism in natural scenes," *J. Opt. Soc. Am. A* **23**, 2359–2372 (2006).
5. G. Lu and B. Fei, "Medical hyperspectral imaging: A review," *J. Biomed. Opt.* **19**, 010901 (2014).
6. S. Grusche, "Basic slit spectroscopy reveals three-dimensional scenes through diagonal slices of hyperspectral cubes," *Appl. Opt.* **53**, 4594–4603 (2014).
7. S. Blais-Ouellette, O. Daigle, and K. Taylor, "The imaging Bragg tunable filter," *Proc. SPIE* **6269**, 62695H (2006).
8. F. Yasuma, T. Mitsunaga, D. Iso, and S. K. Nayar, "Generalized assorted pixel camera: postcapture control of resolution, dynamic range, and spectrum," *IEEE Trans. Image Process.* **19**, pp. 2241–2253 (2010).
9. Z. Pan, G. E. Healey, M. Prasad, and B. J. Tromberg, "Hyperspectral face recognition under variable outdoor illumination," *Proc. SPIE* **5425**, 520–529 (2004).
10. Photon Etc., "Hyperspectral camera V-EOS," Canada, <http://www.photonetc.com/hyperspectral-camera-v-eos>.
11. S. Blais-Ouellette, E. Wishnow, P. Shopbell, W. van Breugel, K. Taylor, and R. Smith, "Double Bragg grating tunable filter," *Proc. SPIE* **492**, 779–786 (2004).
12. S. Barden, J. Williams, J. Arns, and W. Colburn, "Tunable gratings: imaging the universe in 3-D with volume-phase holographic gratings," in *Imaging the Universe in Three Dimensions. Proceedings of the Astronomical Society of the Pacific (ASP)* (2000), Vol. **195**, pp. 552–563.
13. C. E. Shannon, "Communication in the presence of noise," *Proc. IEEE* **86**, 447–457 (1998).
14. A. A. Lacis and J. Hansen, "A parameterization for the absorption of solar radiation in the earth's atmosphere," *J. Atmos. Sci.* **31**, 118–133 (1974).
15. S. Pertuz, D. Puig, and M. A. Garcia, "Analysis of focus measure operators for shape-from-focus," *Pattern Recogn.* **46**, 1415–1432 (2013).
16. E. Krotkov and J. P. Martin, "Range from focus," *Proc. IEEE* **3**, 1093–1098 (1986).
17. W. Ralf, M. M. Blouke, A. Weber, A. Rest, and E. Bodegom, "Temperature dependence of dark current in a CCD," *Proc. SPIE* **4669**, 193–201 (2002).
18. M. Stanton, W. C. Phillips, Y. Li, and K. Kalata, "Correcting spatial distortions and nonuniform response in area detectors," *J. Appl. Crystallogr.* **25**, 549–558 (1992).
19. T. Eckhard, J. Eckhard, E. M. Valero, and J. L. Nieves, "Nonrigid registration with free-form deformation model of multilevel uniform cubic B-splines: application to image registration and distortion correction of spectral image cubes," *Appl. Opt.* **53**, 3764–3772 (2014).
20. G. Sharma, W. Wu, and E. N. Dalal, "The CIEDE2000 color-difference formula: Implementation notes, supplementary test data, and mathematical observations," *Color Res. Appl.* **30**, 21–30 (2005).
21. J. Hernández-Andrés, J. Romero, and R. L. Lee, Jr., "Colorimetric and spectroradiometric characteristics of narrow-field-of-view clear skylight in Granada, Spain," *J. Opt. Soc. Am. A* **18**, 412–420 (2001).
22. Color Imaging Lab, "UGR hyperspectral image database," University of Granada, Spain, http://www.ugr.es/local/colorimg/UGR_hyperspectral_image_database.html.